machines

MDPI

Article

Improved Optimized Minimum Generalized L_p/L_q Deconvolution and Application to Bearing Fault Detection

Na Yang [1,*], Zhigang Pan [2] and Yuanbo Xu [2]

[1] School of Computer Science, Xijing University, Xi'an 710123, China
[2] School of Automation, Xi'an University of Posts and Telecommunications, Xi'an 710121, China; panzhigang@xupt.edu.cn (Z.P.); xuyuanbo@xupt.edu.cn (Y.X.)
* Correspondence: 18165282554@163.com

Abstract: Locating the fault-induced cyclic impulses from corrupted vibration signals is a key step in detecting bearing fault characteristics. Recently, a novel deconvolution technique named the optimized minimum generalized L_p/L_q deconvolution (OMGD) was proposed and has been validated as a useful technique to highlight the periodic impulses related to bearing faults. However, the performance of the OMGD is associated with the appropriate selection of prior parameters, such as the filter length. In addition, the OMGD faces edge effect issues, leading to a shorter duration of the enhanced signal when compared to the measured signal. To overcome the shortcomings of the OMGD, this study proposes an improved version, termed the IOMGD. The enhanced technique employs an advanced sparrow search algorithm to automatically ascertain the filter length, doing away with the need for a predetermined fixed value. To solve the problem of the edge effect, a data extension technique based on the autoregressive model (AR-DET) is proposed to adaptively recover the length of the filtered signal to match that of the raw signal based on the properties observed at the filtered signal. The IOMGD's superiority over the original OMGD has been substantiated by its performance on various real-world bearing fault datasets. Furthermore, a comparative analysis is performed between the IOMGD and other commonly used bearing fault diagnosis methods, revealing the superiority of the IOMGD.

Keywords: rolling bearing; fault detection; data extension technique; enhanced sparrow search algorithm; improved optimized minimum generalized L_p/L_q deconvolution

check for updates

Academic Editor: Ahmed Abu-Siada

Received: 27 February 2025
Revised: 17 March 2025
Accepted: 24 March 2025
Published: 25 March 2025

Citation: Yang, N.; Pan, Z.; Xu, Y. Improved Optimized Minimum Generalized L_p/L_q Deconvolution and Application to Bearing Fault Detection. *Machines* **2025**, *13*, 270. https://doi.org/10.3390/machines13040270

Copyright: © 2025 by the authors. Licensee MDPI, Basel, Switzerland. This article is an open access article distributed under the terms and conditions of the Creative Commons Attribution (CC BY) license (https://creativecommons.org/licenses/by/4.0/).

1. Introduction

Rotating machinery plays a crucial role in various modern industries, including wind energy, automotive, aerospace, and transportation. These machines serve as the backbone of modern industry by providing a reliable source of power [1,2]. Among the numerous components that constitute rotating machinery, rolling bearings hold immense significance. They facilitate smooth rotation by reducing friction between moving parts and supporting heavy loads. However, due to continuous usage under demanding conditions such as high speeds and heavy loads, rolling bearings are prone to damage [3,4]. This leads not only to costly repairs but also results in production downtimes and schedule delays. Ensuring the proper functioning of rolling bearings is crucial for maintaining operational efficiency and averting potential hazards associated with rotating machinery, as they are integral to the smooth operation of mechanical systems.

When localized faults emerge on the outer ring, inner ring, roller, and cage of a bearing, a sequence of repetitive impulse trains exhibiting modulation phenomena are produced [5].

These fault-induced repetitive impulse trains represent cyclo-stationarity, which is directly associated with specific types of bearing faults. The existence of cyclo-stationarity acts as a vital indicator and assessment standard for identifying bearing defects [6]. Unfortunately, the energy of the repetitive impulsive components is extremely weak, making it difficult to identify them from corrupted signals. To overcome this issue, researchers have been exploring various techniques and methodologies to enhance the detection and analysis of fault impulses. One of the most commonly used approaches is the deconvolution-based method, which can effectively filter out background noise and other vibration interference while enhancing the cyclo-stationarity of fault signals [7]. In essence, the objective of deconvolution-based approaches is to optimize a specific criterion that captures the characteristic of impulsiveness in order to design a finite impulse response (FIR) [8]. One key advantage of using an FIR filter in deconvolution-based methods is its adjustable nature. The FIR coefficients can be freely adjusted using different criteria to satisfy the filtering performance for various types of bearing faults. This flexibility allows researchers to tailor the filter characteristics according to specific diagnostic requirements [9,10].

The minimum entropy deconvolution (MED), as the earliest deconvolution method used in fault diagnosis, takes kurtosis as the health criterion to iteratively obtain the FIR coefficients for signal enhancement [11]. Nevertheless, kurtosis is vulnerable to random impulses and lacks the ability to differentiate between random impulses and fault-induced periodic impulses [12,13]. To address the issue of the MED, McDonald et al. [14] designed an improved kurtosis indicator called correlated kurtosis (CK) to propose a novel deconvolution technique, namely, the maximum correlated kurtosis deconvolution (MCKD). The MCKD has been extensively demonstrated in various fault extraction applications for rotating machines. For instance, in the wind turbine [13,15], planetary gearbox [16], motor bearing [17], and locomotive bearing [18] fields, the MCKD has proven to be highly effective. However, the MCKD has certain limitations in practical applications, particularly the necessity for prior knowledge of fault characteristics and the need for an additional resampling process [18]. To cope with the limitations of the MCKD, McDonald et al. [19] proposed a non-iterative deconvolution technique known as multipoint optimal minimum entropy deconvolution adjusted (MOMEDA). This method employs matrix operations to directly determine the optimal coefficients of the FIR filter by maximizing the multi-D-norm of the filtered signal, eliminating the need for any prior assumptions [20]. Due to its exceptional ability in deconvolution, MOMEDA has been effectively utilized for extracting fault features from rotating machines [21–24]. In addition to the family of the MED, various deconvolution methods based on different health indices, such as the harmonics-to-noise-ratio index [25], cyclo-stationarity index [26], Gini index [27], and periodic noise amplitude ratio index [28], have also been developed in recent years.

Based on the aforementioned discussion, this paper will focus on an alternative deconvolution tool named the optimized minimum generalized L_p/L_q deconvolution (OMGD) [29]. The generalized L_p/L_q serves as an exceptionally potent indicator for assessing impacts caused by bearing faults. Its flexibility surpasses kurtosis and the L_1/L_2 norm, as it can be tailored through two variables: p and q. In fact, both kurtosis and the L_1/L_2 norm can be considered as specific instances within the broader framework of the generalized L_p/L_q [30,31]. Moreover, with the application of an initialization method for the initial value, there is a high probability that the OMGD will achieve convergence toward the globally optimal solution [29]. However, some flaws still remain in the OMGD. On the one hand, the performance of the OMGD heavily depends on the filter length to highlight the fault-related impulse train. Prior knowledge of the characteristics of bearing fault signals is necessary for determining the filter length; however, obtaining such knowledge, including center frequency and resonance frequency, can be challenging.

Therefore, the OMGD cannot automatically calculate the filter length. To mitigate the constraints of the filter design, an enhanced sparrow search algorithm (ESSA) is employed to optimize the OMGD method, thereby determining the optimal filter length. This ESSA involves combining the sine–cosine algorithm with the Cauchy mutation. The ESSA successfully tackles the drawbacks of the original SSA, including its slow convergence rate and insufficient exploration capabilities [32]. By incorporating the ESSA into the OMGD algorithm, the optimal filter length can be automatically determined for a given signal, thus tackling the drawback of subjectively determining the filter length using empirical and trial-and-error approaches.

On the other hand, the edge effect, which results in data loss at the end of the filtered signal, is present in the OMGD. This consequence can result in the loss of crucial information pertinent to bearing faults, especially when data loss spans a considerable period. To overcome this limitation, a data prediction technique based on the autoregressive model (AR model) [33] is introduced to recover the filtered signal in this work. The AR-based data prediction technique utilizes an identical set of AR coefficients for extension, which can preserve the spectral characteristics of the original signal without introducing any additional frequency components. Consequently, the extended signal preserves the trend of the original signal while exhibiting a smoother waveform. The efficacy of the IOMGD is confirmed using some real-world signals obtained from different bearing experiments. The findings highlight the superior performance of the IOMGD in automatically extracting fault characteristics associated with rolling bearings, when compared to the original OMGD and other similar deconvolution techniques.

Based on the previous discussion, the proposed IOMGD technique incorporates the ESSA algorithm and the AR-based data prediction technique to address specific challenges faced by the original OMGD. Some highlights are displayed as follows:

(1) By utilizing the AR-based data prediction technique, the IOMGD can automatically extend the filtered signal according to the features of the filtered signal, thereby avoiding the loss of useful information.
(2) One of the key advantages of the IOMGD is its adaptability in selecting optimal parameters based on changing working conditions. This eliminates blind parameter selection and ensures that the technique remains effective across different scenarios.

The following sections are included in this paper. Section 2 provides an overview of the OMGD and discusses its shortcomings. In Section 3, the IMGD is introduced in detail, including a detailed explanation of the filter length selection and AR-based prediction technique. Moving on to Section 4, we validate the effectiveness of our proposed method by comparing it with the original OMGD using real datasets from different bearing test benches. Finally, the conclusions in Section 5 provide a summary of the findings.

2. Theoretical Basis

2.1. OMGD Technique

The concept of the generalized L_p/L_q measure is a significant development in the field of mathematical analysis. It provides a versatile framework for measuring sparsity in signal processing. By considering different values of p and q, it allows us to tailor the measure according to specific requirements. The generalized L_p/L_q norm can be expressed as follows [30]:

$$J_{p,q}(\mathbf{x}) = \log\left(\frac{q}{p}\right)\frac{\sum_{m=1}^{M}|x_m|^p}{\left(\sum_{m=1}^{M}|x_m|^q\right)^{p/q}} = \log\left(\frac{q}{p}\right)\left(\frac{\|\mathrm{x}\|_{l_p}}{\|\mathrm{x}\|_{l_q}}\right)^p, p > 0, q > 0 \quad (1)$$

where **x** is the filtered signal. The formulation of the optimization problem related to blind deconvolution can be expressed as follows:

$$\text{argmin} J_{p,q}(x), \text{subject to} : \mathbf{y} = \mathbf{x} * \mathbf{g}, \|\mathbf{g}\|_2 = 1 \tag{2}$$

in which **y** represents the collected signal, **g** denotes the filter coefficient, and * is the convolution operator. The ultimate objective of the deconvolution process is to obtain the filtered signal **x**, so Equation (2) can be rewritten as follows:

$$\mathbf{g}_{\text{inv}} = \text{argmin} J_{p,g}(\mathbf{y} * \mathbf{g}_{\text{inv}}), \text{subject to} : \|\mathbf{g}_{\text{inv}}\|_2 = 1 \tag{3}$$

Equation (3) can also be expressed as a Hankel matrix form as follows:

$$\mathbf{x} = \mathbf{H}\mathbf{g}_{\text{inv}}, \mathbf{H} = \begin{bmatrix} y_1 & y_2 & y_3 & \cdots & y_k \\ y_2 & y_3 & y_4 & \cdots & y_{k+1} \\ y_3 & y_4 & y_5 & \cdots & y_{k+2} \\ \vdots & \vdots & \vdots & \cdots & \vdots \\ y_{N-k+1} & y_{N-k+2} & y_{N-k+3} & \cdots & y_N \end{bmatrix} \tag{4}$$

where **H** denotes a Hankel matrix.

Similarly, Equation (4) can also be defined as follows:

$$\underset{\mathbf{x},\mathbf{g}_{\text{inv}}}{\text{argmin}} J_{p,g}(\mathbf{x}), \text{subject to} : \mathbf{x} = \mathbf{H}\mathbf{g}_{\text{inv}}, \|\mathbf{g}_{\text{inv}}\|_2 = 1, p < q \tag{5}$$

The gradient descent method can be utilized to solve the optimization problem presented in Equation (5). Based on the backpropagation algorithm, the first derivative can be mathematically represented as follows:

$$\frac{\partial J_{p,q}^i}{\partial \mathbf{g}_{\text{inv}}} = \frac{\partial J_{p,q}^i}{\partial \mathbf{u}^i} \cdot \frac{\partial \mathbf{u}^i}{\partial \mathbf{c}^i} \cdot \frac{\partial \mathbf{c}^i}{\partial \mathbf{x}^i} \cdot \frac{\partial \mathbf{x}^i}{\partial \mathbf{g}_{\text{inv}}} \tag{6}$$

where

$$\frac{\partial J_{p,q}^i}{\partial \mathbf{u}^i} = p \cdot \left(\mathbf{u}^i\right)^{(p-1)} \tag{7}$$

$$\frac{\partial \mathbf{u}^i}{\partial \mathbf{c}^i} = \left[\left(\left\| \mathbf{c}^i \right\|_p \right)^{(1-p)} \cdot \left(\mathbf{c}^i \right)^{(p-1)} \cdot \left\| \mathbf{c}^i \right\|_q - \left(\left\| \mathbf{c}^i \right\|_q \right)^{(1-q)} \cdot \left(\mathbf{c}^i \right)^{(q-1)} \cdot \left\| \mathbf{c}^i \right\|_p \right] \Big/ \left(\left\| \mathbf{c}^i \right\|_q \right) \tag{8}$$

$$\frac{\partial \mathbf{c}^i}{\partial \mathbf{x}^i} = \mathbf{x}^i / \mathbf{c}^i \tag{9}$$

$$\frac{\partial \mathbf{x}^i}{\partial \mathbf{g}_{\text{inv}}} = \mathbf{H}(i, :) \tag{10}$$

The derivative of the entire sample set can be expressed as follows:

$$\frac{\partial J_{p,q}}{\partial \mathbf{g}_{\text{inv}}} = \sum_{i=1}^{N-k+1} \frac{\partial J_{p,q}}{\partial \mathbf{u}^i} \cdot \frac{\partial \mathbf{u}^i}{\partial \mathbf{c}^i} \cdot \frac{\partial \mathbf{c}^i}{\partial \mathbf{x}^i} \cdot \frac{\partial \mathbf{x}^i}{\partial \mathbf{g}_{\text{inv}}{}^i} \tag{11}$$

Initializing an initial value is pivotal for executing gradient descent, as it has a direct bearing on achieving the optimal solution. In the sparse filtering approach, the initial value is randomly assigned. Therefore, it still remains susceptible to being trapped in a local optimal solution. To address this issue, a special initialization procedure [29] is used. The detailed procedures are outlined as follows:

(1) Determine the number of decomposition levels m and the length of the filter L. Define k and L parameters and a generalized L_p/L_q norm;
(2) Similar to spectral kurtosis (SK), based on the frequency plane paving technique for the 1/3-binary tree, the upper and lower frequencies of the filters are determined, and corresponding FIR filters are designed;
(3) The initial values of the deconvolution algorithm are set to be the coefficients of the filters designed in step 2, aiming to optimize the optimal inverse filters.

2.2. Flaws of the OMGD

Undoubtedly, the OMGD exhibits an excellent performance advantage in effectively identifying weak fault characteristics from heavily corrupted signals when compared to some existing deconvolution methods. These findings highlight the superior capability of the OMGD. However, the necessity arises for manual selection of the filter length, a pivotal piece of prior knowledge that must be predetermined. In other words, the determination of the filter length heavily depends on the artificial experience instead of an automatic identification process, thereby hindering its potential for widespread applications.

Another flaw in the OMGD technique is that the enhanced signal suffers from data loss, meaning that the enhanced signal is shorter than the raw signal. The phenomenon of data loss can lead to the loss of critical information related to bearing faults, especially when the duration of missing data is prolonged.

3. Improved OMGD

To address the limitations of the OMGD, an improved OMGD (IOMGD) is proposed. Firstly, this study explores a commonly employed optimization framework for parameter selection for the filter length. The framework utilizes ESSA to optimize the parameter values of the filer length for the OMGD. Additionally, an AR-based data prediction technique is designed to recover the filtered signal.

3.1. Proposed Methodology

3.1.1. ESSA

In the pursuit of sparrows, variations may arise in both food sources and their locations. Upon discovering a highly advantageous food source, explorers draw a substantial crowd to that specific location. Consequently, this diminishes diversity among explorers and the group as a whole, ultimately becoming ensnared in local optima. Therefore, this study integrates the sine–cosine strategy into the SSA and utilizes the fluctuating patterns of sine–cosine models to determine the positions of explorers. This approach effectively maintains individual diversity among explorers, thereby improving the ability of the original SSA for global search and preventing it from becoming stuck in local optima.

The definition of the step search factor in the sine–cosine strategy is as follows:

$$r_1 = c - \frac{cl}{Iteration_{\max}} \tag{12}$$

In Equation (8), c is a fixed value, l indicates the count of iterations, and $Iteration_{\max}$ denotes the upper limit for iteration counts.

The discoverers have formulated a novel mathematical equation, which can be expressed as follows:

$$X_{i,j}^{t+1} = \begin{cases} \beta \cdot X_{l,j}^{t} + b_1 \cdot \sin b_2 \cdot \left| b_3 \cdot X_{best} - X_{l,j}^{t} \right|, & \mathrm{R}_2 < ST \\ \beta \cdot X_{l,j}^{t} + b_1 \cdot \cos b_2 \cdot \left| b_3 \cdot X_{best} - X_{l,j}^{t} \right|, & \mathrm{R}_2 \geq ST \end{cases} \tag{13}$$

where

$$\beta = \frac{e^{\frac{t}{Iteration_{\max}}} - 1}{e - 1} b_2 \in [0, 2\pi] \text{ and } b_3 \in [0, 2\pi] \tag{14}$$

To mitigate the problem of encountering local optima, the Cauchy mutation strategy is introduced into the follower equation of the original SSA, resulting in a modified follower equation as an alternative approach.

$$X_{l,j}^{t+1} = X_{best}(t) + \text{Cauchy}(0, 1) \cdot X_{best}(t) \tag{15}$$

where the standard Cauchy distribution is denoted by Cauchy (0, 1).

The Cauchy distribution shares similarities with the normal distribution, yet it features a more flattened curve and demonstrates a gradual decline toward zero convergence. As a result, introducing variations in the position updates of sparrows within a population, adhering to the Cauchy distribution, can significantly broaden the algorithm's exploration scope. This, in turn, minimizes the risk of the algorithm becoming trapped in local optima. It is important to mention that we provide only a brief overview of these enhancements. Interested readers may refer to [32] for further details.

For a comprehensive evaluation of the ESSA optimization capabilities, a standard test function is implemented to test its efficiency. Alongside the original SSA, two other prevalent optimization algorithms, the Particle Swarm Optimization (PSO) and the Grey Wolf Optimizer (GWO), are utilized to contrast with the ESSA. The standard test function, which acts as the benchmark for this assessment, is outlined as follows:

$$F(x) = \sum_{i=1}^{d} x_i^2 + \left(\sum_{i=1}^{d} 0.5 i x_i\right)^2 + \left(\sum_{i=1}^{d} 0.5 i x_i\right)^4 \text{ interval } [-5, 10] \text{ min } 0 \tag{16}$$

The function F(x) and the convergence behavior of each optimization algorithm are depicted in Figure 1a,b. The results shown in Figure 1b indicate that ESSA possesses an extraordinarily swift convergence rate and achieves a high degree of precision in the evaluation of the function compared to the PSO, SSA, and GWO.

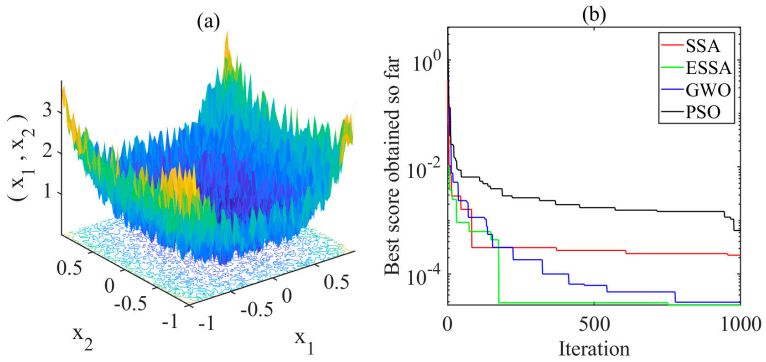


Figure 1. Convergence process of each optimization method. (**a**) Function F(x) and (**b**) convergence behavior.

3.1.2. Objective Function

The selection of the objective function is a crucial step in parameter selection. To account for the impact characteristics of bearing fault signals, we utilize a dimensionless index called the crest factor of the envelope spectrum (CFES) [30] as our chosen objective function. The CFES, being based on frequency domain analysis, demonstrates resistance to

random impulses. A higher CFES value indicates a stronger signal-to-noise ratio (SNR) and more repetitive fault impacts in the filtered signals. Thus, we define the CFES as follows:

$$\text{CFES} = \frac{\max(A[f(x)])}{\sqrt{\sum_x A[f(x)]^2 / x}} \tag{17}$$

where $A[f(x)]$ denotes the amplitude of the effective frequency in the envelope spectrum. The objective function, which utilizes the CFES index, can be formulated as follows:

$$\begin{cases} \text{Objective function} = \underset{\text{Filter length } L}{\arg\max}(\text{CFES}) \\ \text{s.t. } L \in [10\ 500] \end{cases} \tag{18}$$

3.2. AR-Based Data Prediction Technique

AR models, as integral components of ARIMA, are fundamental and widely used methodologies in time series analysis. The AR models evolved from linear regression techniques. The structure of AR models is characterized by a stochastic differential equation, enabling them to elucidate the underlying patterns and regularities within dynamic datasets. They facilitate a quantitative analysis of linear correlations among observed data while also providing predictive insights into future values [33].

A general AR model expression for a signal $s(n)$ can be modeled as follows:

$$s(n) = \sum_{l}^{b} a_l s(n-l) + u(n) \tag{19}$$

where b denotes the order of the model, a_l denotes the prediction coefficient, and $u(n)$ is the noise. The predicted signal can be expressed as follows:

$$\hat{s}(n) = \sum_{i=1}^{b} a_i s(n-i) \tag{20}$$

The most common approach for estimating the coefficients of the AR model a_l involves utilizing autocorrelation, which is a statistical characteristic related to second-order properties of the signal. The Yule–Walker equations are fulfilled by the AR process.

In matrix form,

$$\begin{bmatrix} r(0) & r(1) & r(2) & \cdots & r(b-1) \\ r(1) & r(0) & r(-1) & \cdots & r(b-2) \\ r(2) & r(1) & r(0) & \cdots & r(b-3) \\ \vdots & \vdots & \vdots & \ddots & \vdots \\ r(b-1) & r(b-2) & r(b-3) & \cdots & r(0) \end{bmatrix} \begin{bmatrix} a_1 \\ a_2 \\ a_3 \\ \vdots \\ a_b \end{bmatrix} = \begin{bmatrix} r(1) \\ r(2) \\ r(3) \\ \vdots \\ r(b) \end{bmatrix} \tag{21}$$

The values of r can be obtained using the biased autocorrelation estimate expressed as follows:

$$r(l) = \frac{1}{M} \sum_{m=0}^{M-1} s(n)s(n-l) \tag{22}$$

where M denotes the number of sampling points. The coefficients of the AR model a_l in Equation (11) can be obtained by solving the Yule–Walker equations in Equation (13). The Yule–Walker equations can be solved using various computational methods. In this work, a commonly accepted method named the Levinson–Durbin recursion (LDR) algorithm is used. For a more comprehensive understanding of LDR, please refer to reference [34].

To examine the AR-based prediction technique, a group of simulated bearing fault impulses is employed. The impulse train is shown in Figure 2.

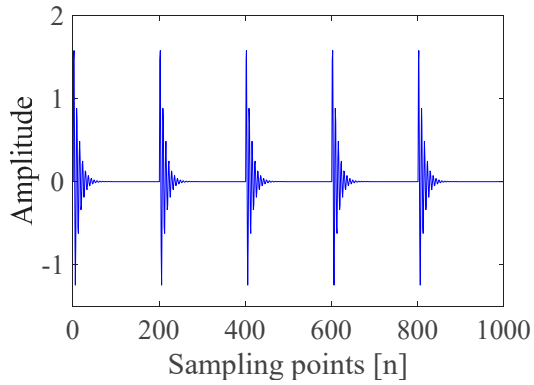


Figure 2. Simulated impulse train.

Figure 3 plots the comparative result between a predicted impulse and an original impulse. Furthermore, the root mean square error (RMSE) index is employed for the assessing quantification of prediction results. It can be observed that the predicted signal and the original signal exhibit a high degree of similarity in their trends, although they did not align perfectly. Meanwhile, the RMSE between the predicted impulse and the original impulse is relatively small (RMSE = 0.20043). Consequently, the AR-based data extension technique can effectively restore the signal by leveraging the inherent characteristics of the original signal.

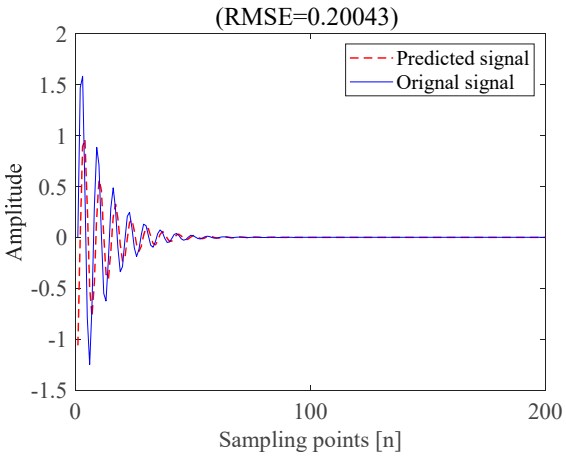


Figure 3. Comparative result.

3.3. Improved OMGD Algorithm

According to the aforementioned discussion, the proposed IOMGD technique utilizes an ESSA approach to automatically determine the filter length without prior knowledge. Furthermore, an AR-based data extension technique is developed to adaptively restore the filtered signal to its original length. The detailed procedure of the IOMGD is listed as follows:

Step 1: Collect the original signal emitted by the defective bearing;

Step 2: Determine the optimization ranges of the IOMGD and initialize the parameters of the ESSA, such as m for the maximum iteration count and n for the number of search agents;

Step 3: Initialize the coefficient g0 using a special initialization procedure;

Step 4: Calculate the Hankel matrix **H** and the inverse filter ginv using Equation (6);

Step 5: Obtain the deconvolved signal $\mathbf{x} = \mathbf{H}\mathbf{g}_{inv}$;

Step 6: Use the AR-based prediction technique to extend the deconvolved signal;

Step 7: Consider the extended signal as a new input for deconvolution, calculate the fitness value of the extended signal, and update the optimal parameters during each iteration of ESSA;

Step 8: Check if the termination condition is satisfied. If yes, conclude the iteration. Otherwise, repeat Steps 2 to 6;

Step 9: Obtain the optimal extended signal $\mathbf{x}$;

Step 9: Detect the fault characteristics using envelope analysis for final fault diagnosis.

The flowchart of the proposed IOMGD is illustrated in Figure 4.

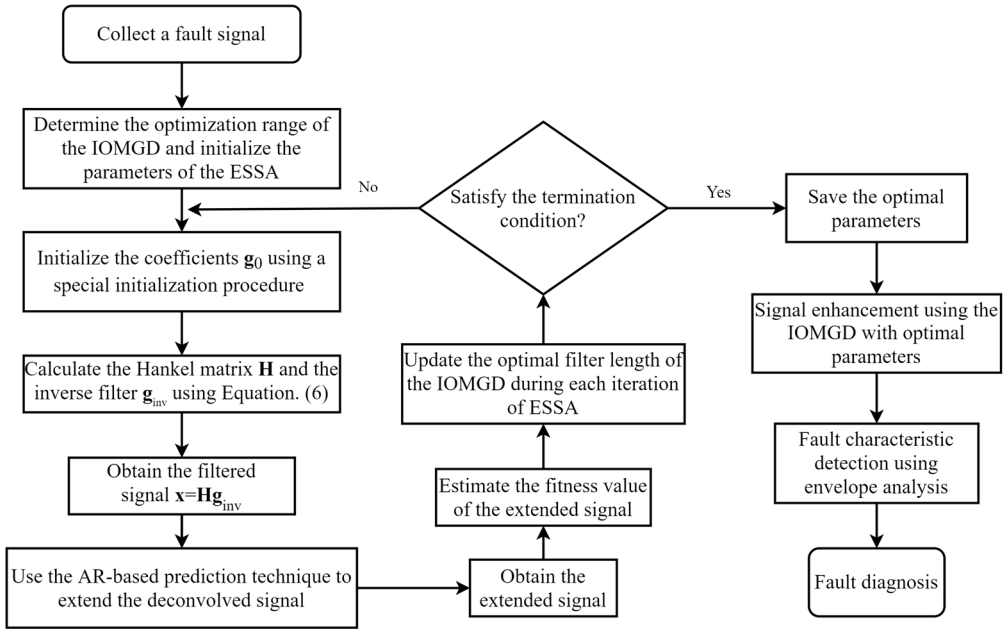


Figure 4. Flowchart of the proposed IOMGD.

4. Case Verification

In this section, we validate the performance of our proposed method by utilizing real bearing fault signals extracted from two different test rigs. To provide a thorough evaluation that shows the strengths of our proposed method, we also conduct a comprehensive comparative analysis with the original OMGD and other competing deconvolution methods.

4.1. Case A: Bearing with an Outer Ring Defect

The real outer ring fault signal was recorded from a YK1022-type circle vibrating screen. The experimental setup, as depicted in Figure 5, is composed of four main sections: the screen box, exciter, support device, and motor. Each corner of the screen features four springs, ensuring its stability and smooth operation. The belt transmissions and two motors drive the entire system. To capture fault signals accurately, accelerometers are strategically placed on the housing of the bearing seat. These accelerometers serve to record any abnormal vibrations or deviations from normal operation. In addition to this setup, two large eccentric blocks are installed on the shaft to generate deterministic components with high energy levels.

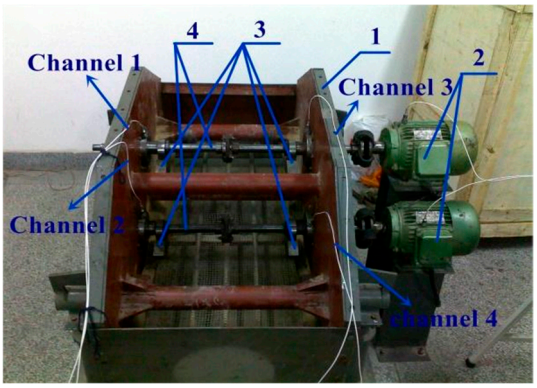


Figure 5. Vibrating screen test rig.

To ensure accurate data acquisition during experimentation, vibration signals were measured at a sampling frequency of 20 kHz while maintaining a constant rotating speed of 1000 rpm (f = 16.67 Hz). The number of sampling points is 10,000. The fault bearing's specifications can be found in Table 1. Therefore, the frequency of the characteristic fault in the outer ring is determined to be BPFO = 104.24 Hz from the parameters in Table 1.

Table 1. Bearing parameters.

Number of balls	15
Ball Diameter (mm)	12.5
Pitch Diameter (mm)	65
Contact angle (°)	30

The waveform of the outer ring fault signal, as shown in Figure 6a, exhibits a distinct influence from the periodic component caused by the rotational movement of the shaft.

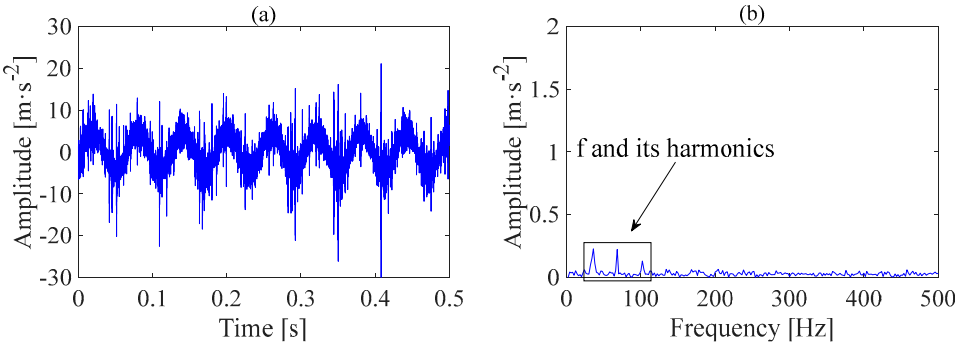


Figure 6. Outer ring fault signal. (**a**) Waveform and (**b**) its envelope spectrum.

This periodicity leads to fluctuations and variations in the waveform, thereby posing significant challenges in accurately identifying and analyzing the underlying fault information. The presence of strong ambient noise further complicates the analysis process. Furthermore, as shown in Figure 6b, the envelope spectrum is mainly influenced by the rotating frequency f and its harmonics, making the presence of BPFO undetectable.

The fault signal is processed using the proposed IOMGD method. This improved algorithm allows for accurate parameter selection. The convergence curve is depicted in Figure 7. The maximum fitness value achieved during this process is recorded at 7.6157. The corresponding solution that yielded this result is found to be $L = 30$.

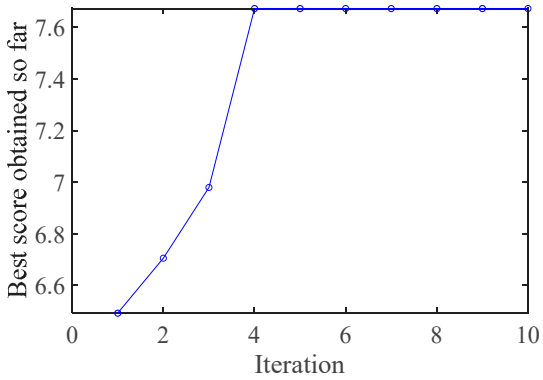


Figure 7. Iteration process.

Figure 8 plots the enhanced signal achieved through the utilization of the IOMGD method with an optimal parameter value of L = 30 and its corresponding envelope spectrum. The results are quite remarkable, as they clearly demonstrate the successful elimination of periodic vibration components and a significant reduction in background noise. This enhancement effectively amplifies the fault impulses present in the filtered signal. Moving on to the envelope spectrum, we can obviously observe that the envelope spectrum provides the BPFO at 104.25 Hz, along with its subsequent harmonics at 2BPFO and 3BPFO.

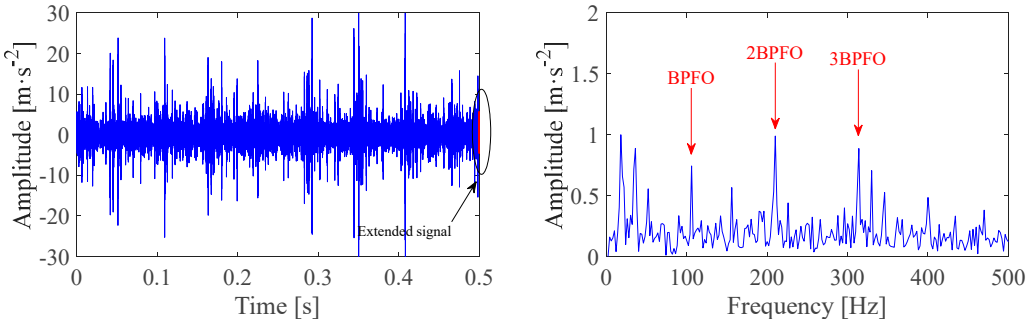


Figure 8. Fault detection results.

To demonstrate the influence of filter length on fault signature detection, we also employed the original OMGD with filter lengths of 80, 120, and 200 to analyze the outer ring fault signal, as illustrated in Figure 9. Examining the waveform of the filtered signals reveals a significant data loss issue, indicating that vital information may be omitted or distorted, potentially compromising the accuracy and reliability of subsequent analyses. Furthermore, examination of the envelope spectra reveals that various filter lengths have a direct influence on the performance of the OMGD. The OMGD techniques with three different filter lengths are able to, respectively, identify the BPFO and its first two harmonics. Nevertheless, it becomes apparent that these results are less satisfactory when compared to those achieved using the IOMGD with an optimized filter length. Therefore, optimizing this parameter within the OMGD algorithm has the potential to improve detection capabilities.

It should be noted that we do not discuss the influence of data loss on fault feature detection in this section, because the optimal filter length of L = 30 is relatively small compared to the length of the original signal. The limited extent of data loss has a small impact on fault identification.

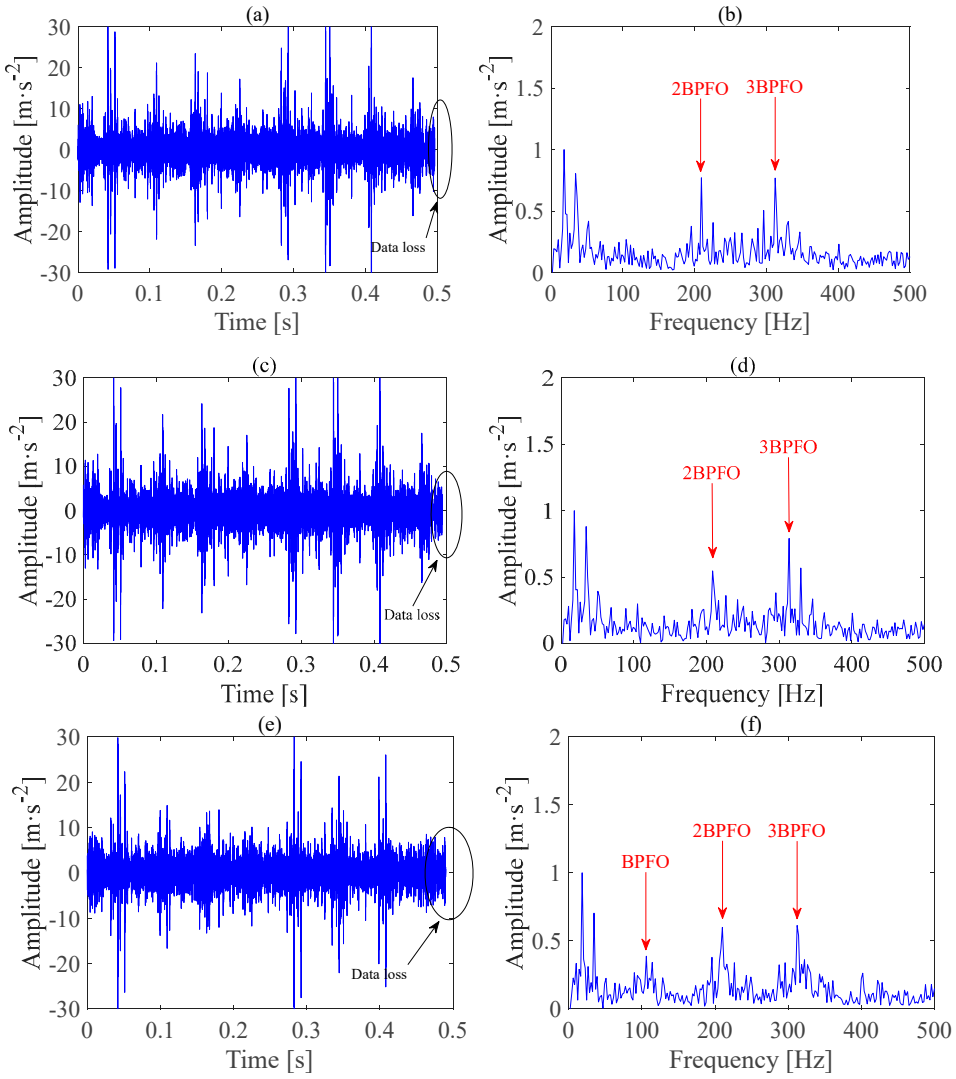


Figure 9. Filtered signals using OMGD with different L. (**a**) Waveform in the case of L = 80; (**b**) envelope spectrum in the case of L = 80; (**c**) waveform in case of L = 120; (**d**) envelope spectrum in the case of L = 120; (**e**) waveform in case of L = 200; (**f**) envelope spectrum in the case of L = 200.

4.2. Case B: Bearing with an Inner Ring Defect

In the second experiment, a gearbox test bench provided by the LASPI laboratory in France [35] was utilized, as depicted in Figure 10. The main component of interest is the asynchronous cage motor, which drives a three-axis gearbox. This gearbox consists of three rotating shafts that play crucial roles in transmitting power and controlling motion. Starting with the input shaft, it is directly driven by the rotor shaft of the motor. Moving along to the output shaft, we find an electromagnetic brake positioned strategically to apply a load level on the motor.

The pulse generator controls the motor's speed by altering the rotational frequencies (25 Hz, 35 Hz, and 45 Hz). The conducted experiments involve four different load levels (0%, 25%, 50%, and 75%) at varying speeds. For this experiment, we focused on the working conditions with a rotating frequency of 45 Hz and a load level of 0%. Table 2 lists the characteristic parameters of the defective bearing. Consequently, the frequency associated with faults in the inner race is calculated to be BPFI = 270.77 Hz.

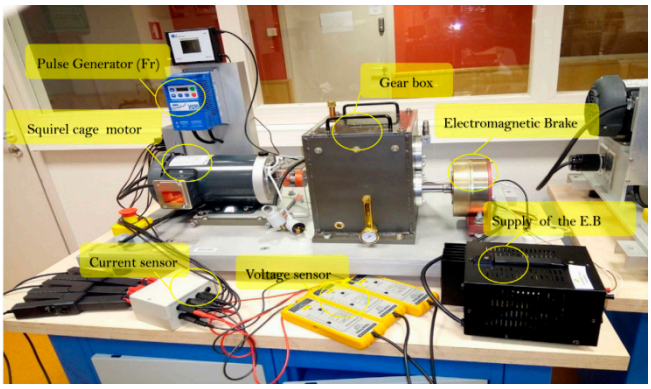


Figure 10. Test bench.

Table 2. Characteristic parameters of the faulty bearing.

Ball diameter (mm)	7.02
Pitch diameter (mm)	18.65
Number of rolling elements	9
Contact angle	0°

The fault signal extracted from the inner ring is given in Figure 11a,b, which show the corresponding envelope spectrum. The fault signal is affected by strong interference. Furthermore, the envelope spectrum does not provide a clear indication of this BPFI, only showing the rotating frequency and its first harmonics.

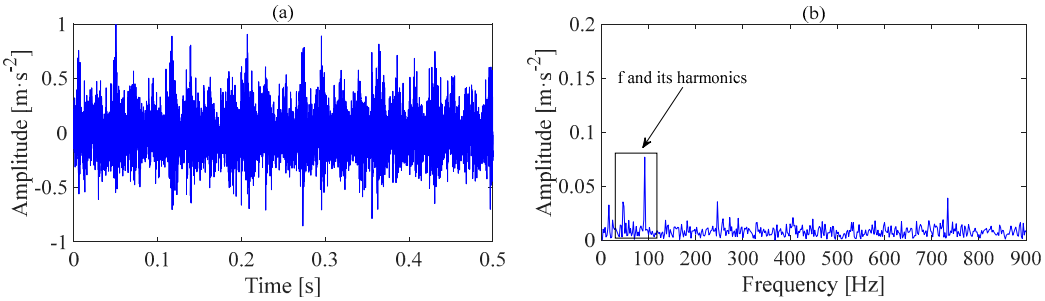


Figure 11. Fault signal collected from the inner ring. (**a**) Time-domain waveform and (**b**) its envelope spectrum.

The IOMGD technique is now used to enhance the fault signal. As before, in order to achieve optimal performance, the predefined parameters of this technique need to be optimized using the ESSA. The resulting optimization curve is depicted in Figure 12. After thorough optimization using ESSA, we obtain the optimal values for the crucial parameters L = 320 when the fitness value is 6.8917.

Figure 13 depicts the filtered signal using the IOMGD with optimal filter length and its corresponding envelope spectrum. We can observe that the IOMGD effectively eliminates the vibration interference and noise, allowing us to focus solely on the fault cyclic impulses. In addition, the predicted signal can better match the filtered signal. As anticipated, the corresponding envelope spectrum provides a clear visualization of the BPFI and its first three harmonics.

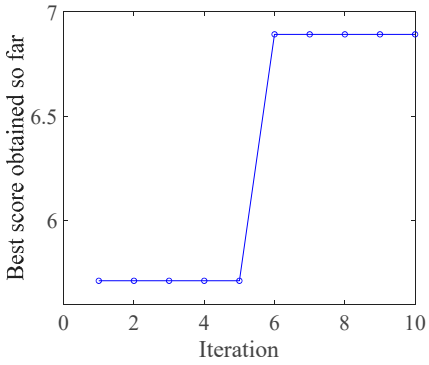


Figure 12. Convergence curve.

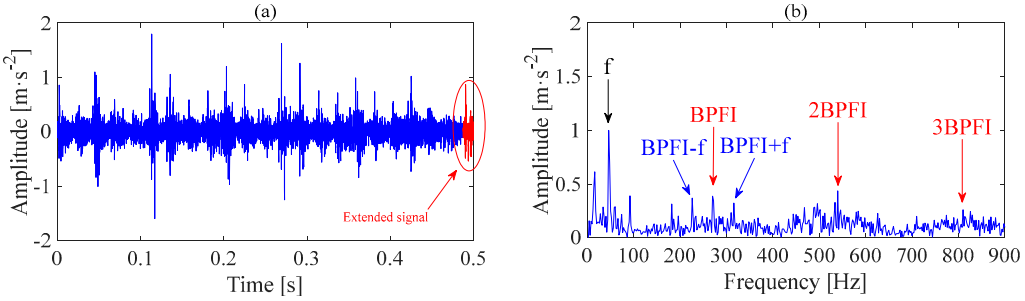


Figure 13. IOMGD-enhanced signal. (**a**) Time-domain waveform and (**b**) its envelope spectrum.

To further demonstrate the impact of data loss on fault detection, we also utilize the original OMGD method with an optimal L = 320 to process the fault signal. In Figure 14, we present the filtered signal and its corresponding envelope spectrum. It is evident that, in the presence of data loss, the OMGD algorithm is still capable of identifying the BPFI. However, it becomes challenging to observe the second harmonic of the BPFI due to this reduction in available data. Consequently, this decrease in information may have a certain influence on accurately extracting fault features from the filtered signal.

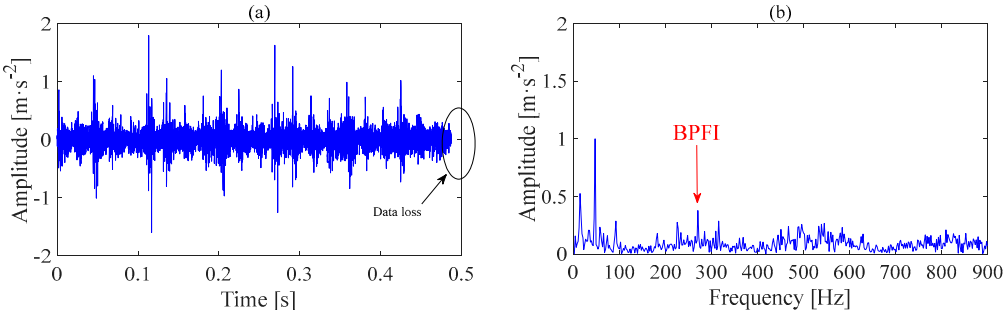


Figure 14. OMGD-enhanced signal. (**a**) Time-domain waveform and (**b**) its envelope spectrum.

Finally, to further validate the superiority of the proposed IOMGD, some existing deconvolution methods, such as MED, MCKD [14], and MNAD [28], are used for comparison with the IOMGD. For a comprehensive comparative analysis, the ESSA algorithm is also integrated with these deconvolution methods to optimize the filter length. The results obtained using these optimized deconvolution techniques are presented in Figure 15. According to Figure 15a,c,e, the deconvolution tools have been evaluated for their ability to reduce periodic vibration interference and background noise while enhancing fault-induced cyclic impulses. Although all of the techniques show some level of success, there are still noticeable differences in the final fault extraction results.

The MED technique shows its effectiveness in accurately extracting both the BPFI and the 2BPFI. However, despite its capabilities, the MED technique falls short in detecting the presence of the 3BPFI. On the other hand, the MCKD and the MNAD are only capable of detecting the BPFI and do not perform as well when it comes to identifying other harmonics such as the 2BPFI or the 3BPFI. As a result of a thorough comparative analysis, the proposed IOMGD method clearly demonstrates superior performance. It outperforms the commonly used deconvolution methods by providing more accurate and comprehensive detection of the BPFI and its harmonics, thus proving to be a more effective tool in the field of signal processing and fault diagnosis.

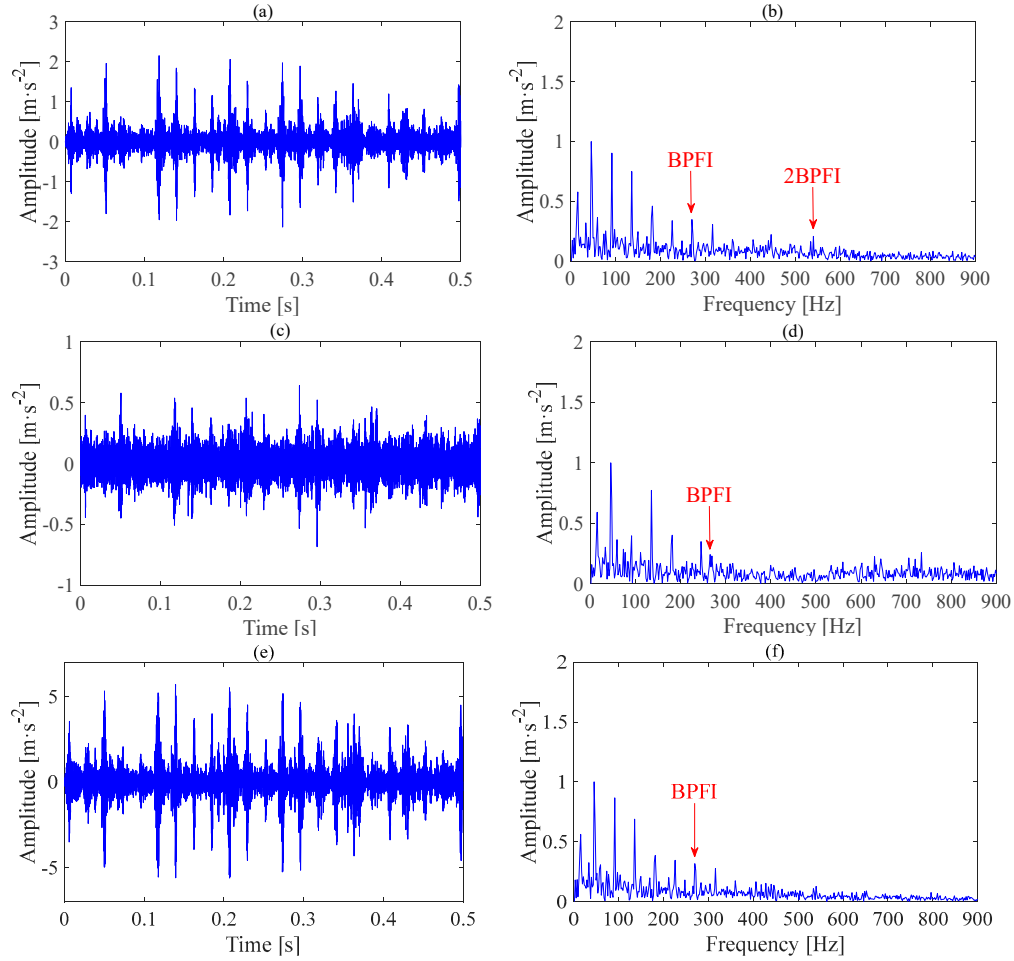


Figure 15. Final enhanced signal. (**a**) MED-filtered signal, (**b**) its envelope spectrum, (**c**) MCKD-filtered signal, (**d**) its envelope spectrum, (**e**) MNAD-filtered signal, and (**f**) its envelope spectrum.

In order to quantitatively evaluate these outcomes, a metric referred to as the Fault Feature Coefficient (FFC) [36] is introduced. This metric functions as a powerful instrument for the assessment and quantification of fault characteristics. The employment of the FFC facilitates an objective measurement of fault detection performance. The FFC is defined as follows:

$$P_{FFC} = \frac{\sum[Am(f)]^2}{\sum[Am(F)]^2} \times 100\% \tag{23}$$

where P_{FFC} represents the ratio of fault-related energy to total spectral energy. $A_{\mathrm{m}}(f)$ denotes the magnitude of fault-related components, while $A_{\mathrm{m}}(F)$ indicates the overall amplitude of frequency components in the envelope spectrum. Table 3 displays the *FFC* values of the four deconvolution methods. We observe that the FFC values generated by the three deconvolution tools are all below 22.6%, as determined by the IOMGD method.

Table 3. FFC values.

Method	FFC Value
IOMGD method	22.6%
MED method	11.7%
MCKD method	8.3%
MNAD method	9.1%

5. Conclusions

This paper proposes an improved OMGD technique to enhance the corrupted signal. The proposed IOMGD technique incorporates the ESSA algorithm and the AR-based data prediction technique to address specific challenges faced by the original OMGD. Leveraging AR-based data prediction, the IOMGD can dynamically extend the filtered signal by analyzing its characteristics, thus preserving valuable information. Furthermore, one of the key advantages of the IOMGD is its adaptability in selecting optimal parameters based on changing working conditions. This eliminates blind parameter selection and ensures that the technique remains effective across different scenarios. To validate its effectiveness in bearing fault detection, two sets of actual bearing fault data are analyzed using the IOMGD. Moreover, to provide a comprehensive evaluation of the IOMGD's superiority, a comparative study is conducted involving not only the original OMGD but also various deconvolution approaches available in the literature. The results confirmed that this proposed approach outperforms other existing deconvolution methods.

However, it should be noted that, due to its reliance on ESSA for estimating optimal values, particularly when dealing with large volumes of fault data, there may be a time requirement associated with implementing this technique effectively. Further exploration is needed to address this issue and potentially optimize computational efficiency without compromising accuracy. Furthermore, we will emphasize this limitation and commit to expanded evaluations in future studies, such as compound faults, varying time conditions, and other mechanical elements.

Author Contributions: Conceptualization, methodology, software, validation, funding acquisition and writing—original draft preparation, N.Y. and Y.X.; resources, funding acquisition, writing—review and editing, N.Y. and Z.P. All authors have read and agreed to the published version of the manuscript.

Funding: This study was supported by the Research Fund Project of Xijing University [No. XJ220206] and the Key Research and Development Program of Shaanxi [No. 2023-YBGY-407].

Data Availability Statement: The raw data supporting the conclusions of this article will be made available by the authors upon request.

Conflicts of Interest: The authors declare no conflicts of interest.

References

1. Xu, C.; Li, J.; Cheng, X. Comprehensive Learning Particle Swarm Optimized Fuzzy Petri Net for Motor-Bearing Fault Diagnosis. *Machines* **2022**, *10*, 1022. [CrossRef]
2. Yu, Y.; Karimi, H.; Gelman, L.; Cetin, A. MSIFT: A Novel End-to-End Mechanical Fault Diagnosis Framework under Limited & Imbalanced Data Using Multi-Source Information Fusion. *Expert Syst. Appl.* **2025**, *274*, 126947.
3. Hu, Y.; Tu, X.; Li, F.; Meng, G. Joint High-Order Synchrosqueezing Transform and Multi-Taper Empirical Wavelet Transform for Fault Diagnosis of Wind Turbine Planetary Gearbox under Nonstationary Conditions. *Sensors* **2018**, *18*, 150. [CrossRef]
4. Xiao, C.; Yang, P.; Yue, S.; Zhou, R.; Yu, J. Bearing Compound Fault Diagnosis Using Energy-Constrained Swarm Decomposition and Adaptive Spectral Amplitude Modulation. *IEEE Sens. J.* **2024**, *24*, 18172–18184.
5. Liu, Z.; Jin, Y.; Zuo, M.J.; Peng, D. ACCUGRAM: A Novel Approach Based on Classification to Frequency Band Selection for Rotating Machinery Fault Diagnosis. *ISA Trans.* **2019**, *95*, 346–357. [PubMed]

6. Liu, M.; Shen, Y.; Xu, Y. A Resonance-Identification-Guided Autogram for the Fault Diagnosis of Rolling Element Bearings. *Machines* **2025**, *13*, 169. [CrossRef]
7. Sawalhi, N.; Randall, R.B.; Endo, H. The Enhancement of Fault Detection and Diagnosis in Rolling Element Bearings Using Minimum Entropy Deconvolution Combined with Spectral Kurtosis. *Mech. Syst. Signal Process.* **2007**, *21*, 2616–2633.
8. Jiang, R.; Chen, J.; Dong, G.; Liu, T.; Xiao, W. The Weak Fault Diagnosis and Condition Monitoring of Rolling Element Bearing Using Minimum Entropy Deconvolution and Envelop Spectrum. *Proc. Inst. Mech. Eng. Part C J. Mech. Eng. Sci.* **2013**, *227*, 1116–1129.
9. Chao, J.; Ming, Z.; Jay, L.; Jia, X.; Di, Y. Investigation on the Kurtosis Filter and the Derivation of Convolutional Sparse Filter for Impulsive Signature Enhancement. *J. Sound Vib.* **2017**, *386*, 433–448.
10. Randall, R.B.; Antoni, J. Rolling Element Bearing Diagnostics—A Tutorial. *Mech. Syst. Signal Process.* **2011**, *25*, 485–520.
11. Xu, Y.; Cai, Z.; Cai, X.; Ding, K. An Enhanced Multipoint Optimal Minimum Entropy Deconvolution Approach for Bearing Fault Detection of Spur Gearbox. *J. Mech. Sci. Technol.* **2019**, *33*, 2573–2586. [CrossRef]
12. Cheng, Y.; Wang, Z.; Zhang, W.; Huang, G. Particle Swarm Optimization Algorithm to Solve the Deconvolution Problem for Rolling Element Bearing Fault Diagnosis. *ISA Trans.* **2019**, *90*, 244–267.
13. Miao, Y.; Zhao, M.; Liang, K.; Lin, J. Application of an Improved MCKDA for Fault Detection of Wind Turbine Gear Based on Encoder Signal. *Pergamon* **2020**, *151*, 192–203.
14. Mcdonald, G.L.; Zhao, Q.; Zuo, M.J. Maximum Correlated Kurtosis Deconvolution and Application on Gear Tooth Chip Fault Detection. *Mech. Syst. Signal Process.* **2012**, *33*, 237–255.
15. Zhang, J.; Zhang, J.; Zhong, M.; Zhong, J.; Yao, L. Detection for Incipient Damages of Wind Turbine Rolling Bearing Based on VMD-AMCKD Method. *IEEE Access* **2019**, *7*, 67944–67959.
16. Zhang, J.; Zhong, M.; Zhang, J. Detection for Weak Fault in Planetary Gear Trains Based on an Improved Maximum Correlation Kurtosis Deconvolution. *Meas. Sci. Technol.* **2020**, *31*, 025101.
17. Tang, G.; Wang, X.; He, Y. Diagnosis of Compound Faults of Rolling Bearings through Adaptive Maximum Correlated Kurtosis Deconvolution. *J. Mech. Sci. Technol.* **2016**, *30*, 43–54. [CrossRef]
18. Miao, Y.; Zhao, M.; Lin, J.; Lei, Y. Application of an Improved Maximum Correlated Kurtosis Deconvolution Method for Fault Diagnosis of Rolling Element Bearings. *Mech. Syst. Signal Process.* **2017**, *92*, 173–195.
19. Mcdonald, G.L.; Zhao, Q. Multipoint Optimal Minimum Entropy Deconvolution and Convolution Fix: Application to Vibration Fault Detection. *Mech. Syst. Signal Process.* **2017**, *82*, 461–477.
20. Cheng, Y.; Chen, B.; Zhang, W. Adaptive Multipoint Optimal Minimum Entropy Deconvolution Adjusted and Application to Fault Diagnosis of Rolling Element Bearings. *IEEE Sens. J.* **2019**, *19*, 12153–12164. [CrossRef]
21. Cai, W.; Wang, Z. Application of an Improved Multipoint Optimal Minimum Entropy Deconvolution Adjusted for Gearbox Composite Fault Diagnosis. *Sensors* **2018**, *18*, 2861. [CrossRef] [PubMed]
22. Xu, Y.; Li, Y.; Wang, Y.; Wei, Y.; Li, Z. A Novel Strategy Using Optimized MOMED and B-Spline Based Envelope-Derivative Operator for Compound Fault Detection of the Rolling Bearing. *Struct. Health Monit.* **2022**, *21*, 2569–2586. [CrossRef]
23. Hou, Y.; Zhou, C.; Tian, C.; Wang, D.; He, W.; Huang, W.; Wu, P.; Wu, D. Acoustic Feature Enhancement in Rolling Bearing Fault Diagnosis Using Sparsity-Oriented Multipoint Optimal Minimum Entropy Deconvolution Adjusted Method. *Appl. Acoust.* **2022**, *201*, 109105. [CrossRef]
24. Wang, Z.; Du, W.; Wang, J.; Zhou, J.; Huang, L. Research and Application of Improved Adaptive MOMEDA Fault Diagnosis Method. *Measurement* **2019**, *140*, 63–75. [CrossRef]
25. Miao, Y.; Zhao, M.; Lin, J.; Xu, X. Sparse Maximum Harmonics-to-Noise-Ratio Deconvolution for Weak Fault Signature Detection in Bearings. *Meas. Sci. Technol.* **2016**, *27*, 105004. [CrossRef]
26. Buzzoni, M.; Antoni, J.; d'Elia, G. Blind Deconvolution Based on Cyclostationarity Maximization and Its Application to Fault Identification. *J. Sound Vib.* **2018**, *432*, 569–601. [CrossRef]
27. Miao, Y.; Wang, J.; Zhang, B.; Li, H. Practical Framework of Gini Index in the Application of Machinery Fault Feature Extraction. *Mech. Syst. Signal Process.* **2022**, *165*, 108333. [CrossRef]
28. Fang, B.; Hu, J.; Yang, C. Minimum noise amplitude deconvolution and its application in repetitive impact detection. *Struct. Health Monit.* **2023**, *22*, 1807–1827. [CrossRef]
29. He, L.; Yi, C.; Wang, D.; Wang, F.; Lin, J. Optimized Minimum Generalized Lp/Lq Deconvolution for Recovering Repetitive Impacts from a Vibration Mixture. *Measurement* **2021**, *168*, 108329. [CrossRef]
30. Jia, X.; Zhao, M.; Di, Y.; Li, P.; Lee, J. Sparse Filtering with the Generalized Lp/Lqnorm and Its Applications to the Condition Monitoring of Rotating Machinery. *Mech. Syst. Signal Process.* **2017**, *102*, 198–213. [CrossRef]
31. Zhou, Q.; Zhang, Y.; Tang, J.; Lin, J.; Yi, C. Blind Deconvolution Technique Based on Improved Correlated Generalized Lp/Lq Norm for Extracting Repetitive Transient Feature. *IEEE Trans. Instrum. Meas.* **2021**, *70*, 3519421.
32. Liu, T.; Yuan, Z.; Wu, L.; Badami, B. An Optimal Brain Tumor Detection by Convolutional Neural Network and Enhanced Sparrow Search Algorithm: Proc. *Inst. Mech. Eng. Part H J. Eng. Med.* **2021**, *235*, 459–469.

33. Šmídl, V.; Quinn, A. Mixture-Based Extension of the AR Model and Its Recursive Bayesian Identification. *IEEE Trans. Signal Process.* **2005**, *53*, 3530–3542.
34. Boshnakov, G.N.; Lambert-Lacroix, S. A Periodic Levinson-Durbin Algorithm for Entropy Maximization. *Comput. Stat. Data Anal.* **2012**, *56*, 15–24.
35. Soualhi, M.; Nguyen, K.T.; Soualhi, A.; Medjaher, K.; Hemsas, K.E. Health Monitoring of Bearing and Gear Faults by Using a New Health Indicator Extracted from Current Signals. *Measurement* **2019**, *141*, 37–51.
36. Gu, R.; Chen, J.; Hong, R.; Wang, H.; Wu, W. Incipient Fault Diagnosis of Rolling Bearings Based on Adaptive Variational Mode Decomposition and Teager Energy Operator. *Measurement* **2020**, *149*, 106941.

Disclaimer/Publisher's Note: The statements, opinions and data contained in all publications are solely those of the individual author(s) and contributor(s) and not of MDPI and/or the editor(s). MDPI and/or the editor(s) disclaim responsibility for any injury to people or property resulting from any ideas, methods, instructions or products referred to in the content.